Voltage cycling process for the electroconversion of biomass-derived polyols

Dohyung Kim[a], Chengshuang Zhou[a], Miao Zhang[b], and Matteo Cargnello[a,c,1]

[a]Department of Chemical Engineering, Stanford University, Stanford, CA 94305; [b]Chemical Sciences Division, Lawrence Berkeley National Laboratory, Berkeley, CA 94720; and [c]SUNCAT Center for Interface Science and Catalysis, Stanford University, Stanford, CA 94305

Edited by Alexis T. Bell, University of California, Berkeley, CA, and approved September 2, 2021 (received for review July 20, 2021)

Electrification of chemical reactions is crucial to fundamentally transform our society that is still heavily dependent on fossil resources and unsustainable practices. In addition, electrochemistry-based approaches offer a unique way of catalyzing reactions by the fast and continuous alteration of applied potentials, unlike traditional thermal processes. Here, we show how the continuous cyclic application of electrode potential allows Pt nanoparticles to electrooxidize biomass-derived polyols with turnover frequency improved by orders of magnitude compared with the usual rates at fixed potential conditions. Moreover, secondary alcohol oxidation is enhanced, with a ketoses-to-aldoses ratio increased up to sixfold. The idea has been translated into the construction of a symmetric single-compartment system in a two-electrode configuration. Its operation via voltage cycling demonstrates high-rate sorbitol electrolysis with the formation of H_2 as a desired coproduct at operating voltages below 1.4 V. The devised method presents a potential approach to using renewable electricity to drive chemical processes.

electroconversion | polyols | voltage cycling | platinum

A major element in future sustainable scenarios is electrification. The replacement of the usual carbon-heavy processes with renewable electricity-driven approaches is seen as a way to reduce their carbon footprint and decarbonize our society (1, 2). Therefore, much progress has been made in how electrical energy is produced, stored, and converted (3). Furthermore, there has been growing interest to electrify the chemical sector responsible for a significant portion of products used worldwide (4–12). Electrochemistry-based approaches can avoid the use of chemical oxidants and thermochemical treatments that are energy intensive and unsustainable. Moreover, electrocatalytic routes potentially offer finer control over reaction pathways thanks to their nature of bond activation mediated by electrons at electrode surfaces, in contrast to thermocatalytic methods, in which temperature indiscriminately disrupts multiple chemical bonds simultaneously in a single molecule.

For electrochemical methods to be useful to drive reactions, high reaction rates must be maintained and product selectivity needs to be controlled. Therefore, efforts have largely focused on the design of catalyst materials, from tuning active site motifs to creating large-scale architectures to host active sites (13, 14). Understanding the effects of catalyst structure in thermocatalysis has helped guide catalyst design, as well, by translating similar strategies into electrocatalysis (15–17). However, improvements in catalytic activity have been limited in some of the challenging reactions, and alternative ways for their electrification have been developed, such as using redox mediators (6, 9, 10, 12).

One aspect unique to an electrochemical approach compared with a thermochemical process is the ability to quickly apply and adjust energy to the system, whose response is also rapid. This is often manifested in the form of electrochemical potential pulses. It allows continuously taking advantage of transient states of the system and its surroundings, unlike traditional approaches under steady-state (SS) fixed potential conditions. Potential pulsing has proven useful for the conversion of small molecules such as CO_2 and formic acid. It has been shown to be advantageous in various ways including regeneration of catalytically active defects, removing poisonous species, and altering reaction pathways (18–21). In addition, short potential pulses can take advantage of the periodic renewal of the surrounding environment, which has been demonstrated to be optimal for tuning the selectivity of organic reactions (22–24). It has also been adopted for electropolymerization reactions producing single-molecular polymeric structures (25).

Here, we apply the idea of continuous alteration of potentials to electroconversion of biomass-derived polyols. Biomass-derived polyols are naturally abundant resources such as the six-carbon sorbitol that can be readily obtained from cellulose (26). Their potential as a platform chemical makes them high-value biomass compounds to be utilized through oxidation to various chemicals (27–29). By the continuous cycling of potential applied to sorbitol electroconversion, we find Pt nanoparticles to exhibit intrinsic activity improvements and unusual selectivity shifts compared with fixed potential conditions. Turnover frequency (TOF) is enhanced by an order of magnitude, and secondary alcohol oxidation is promoted with a ketoses-to-aldoses ratio (K/A) increased over sixfold. Similar improvements are demonstrated with other C_3-C_5 polyols as well. Furthermore, we show that potential cycling relies on the high oxidative activity of nonequilibrated Pt surfaces otherwise difficult to maintain in typical conditions. Such knowledge is translated to an electrolyzer in a two-electrode configuration via a method called voltage cycling (VC) (hereafter, voltage refers to the voltage applied between the electrodes in a two-electrode configuration, whereas term potential is used to indicate the applied

Significance

Facilitating electrochemical reactions on heterogeneous surfaces is key to achieving sustainability through renewable electricity-based production of fuels and chemicals. With prior efforts focused on the electroconversion of small molecules (e.g., H_2O and CO_2), advances involving complex molecules that are abundant and of high value, such as biomass-derived compounds, have been limited. This work proposes an electrochemical method, so-called potential cycling, which enables standard Pt nanoparticles to exhibit high activity for electrooxidation of biomass-derived polyols. Turnover is enhanced by orders of magnitude, overcoming the severe limitation of negligible activity exhibited by the same catalyst under typical electrochemical conditions. Moreover, the demonstration of a two-electrode system that couples polyol electrooxidation with water reduction to H_2 highlights the potential applicability of the method.

Author contributions: D.K. and M.C. designed research; D.K. performed research; C.Z. and M.Z. contributed new reagents/analytic tools; D.K. analyzed data; and D.K. and M.C. wrote the paper.

The authors declare no competing interest.

This article is a PNAS Direct Submission.

[1]To whom correspondence may be addressed. Email: mcargnello@stanford.edu.

This article contains supporting information online at https://www.pnas.org/lookup/suppl/doi:10.1073/pnas.2113382118/-/DCSupplemental.

Published October 6, 2021.

potential in a three-electrode configuration) demonstrating sorbitol electrolysis and coproduction of H_2 at fast output rates with applied voltage below 1.4 V.

Results and Discussion

Sorbitol Electrooxidation under Steady-State Conditions. Platinum nanoparticles with an average size of 1.8 nm supported on carbon (Pt/C) served as catalysts (Fig. 1*A* and *SI Appendix*, Fig. S1). Pt/C (40 μg_{Pt}) was loaded onto carbon paper (1 cm^2 geometric area) and used as a working electrode in a typical three-electrode H cell (*SI Appendix*, Fig. S2). With sorbitol present in the electrolyte, a decrease in the hydrogen underpotential deposition current was observed, indicating a loss in the available Pt surface area (*SI Appendix*, Fig. S3). This is due to the dissociative adsorption of sorbitol on Pt to yield $*CO_{ads}$ as previously described (30). A potential-dependent trend of $*CO_{ads}$ formation shows that this process becomes negligible above 0.6 V (*SI Appendix*, Fig. S3). Thus, we found that potentials >0.6 V were necessary to convert sorbitol without CO poisoning the surface of Pt nanoparticles.

Sorbitol contains six hydroxyl groups. Depending on how the oxidation takes place, it can lead to three different product groups that are the aldoses, ketoses, and aldonic acids (Fig. 1*B*). These products were analyzed using high-pressure liquid chromatography–mass spectrometry (HPLC-MS) and calibration standards (*SI Appendix*, Fig. S4). Fig. 1*C* shows that the SS current density for Pt/C biased at 0.7 V in 0.1 M sorbitol solution rapidly declines to <100 $\mu A/cm^2$. Similarly low activities were observed for other potentials beyond 0.7 V (*SI Appendix*, Fig. S5). Such low activity makes continuous, SS oxidation of sorbitol by Pt nanoparticles challenging in aqueous solutions at room temperature and ambient conditions (17, 31). It took an average of ~120 h to reach a sorbitol conversion of ~8% (Fig. 1*D*). The sum of faradaic efficiencies closely matched the charge passed at the Pt/C electrode (*SI Appendix*, Fig. S6). Furthermore, gas products, such as CO_2, were not detected as expected from the lack of dissociative adsorption at these potentials. Aldoses were the main product (60 to 80%), as expected from platinum's known catalytic behavior to oxidize primary alcohols and the more favorable conversion of terminal functional groups (Fig. 1*D* and *SI Appendix*, Fig. S6) (16, 17, 32). At applied potential >1.1 V, the overall behavior of activity/selectivity did not change but CO_2 and formic acid appeared as byproducts (*SI Appendix*, Fig. S7). Such C_1 products have been observed for glycerol oxidation at very positive potentials associated with Pt surface oxides (33). In short, Pt nanoparticles can oxidize sorbitol majorly to aldoses at a very low activity under SS applied potentials.

Electrochemical Potential Cycling Applied to Sorbitol Conversion. To overcome the limitation of SS conversion, we sought to exploit the high transient activity of Pt nanoparticles only observed at the early periods within few seconds (Fig. 1*C* and *SI Appendix*, Fig. S5). Thus, instead of applying a constant fixed potential, we approached in a way called electrochemical potential cycling (EPC) that continuously scans the potential in the range 0.02 to 1.1 V at a scan rate of 100 mV/s (Fig. 2*A*). The approach was motivated by the large discrepancy in current density observed during cyclic voltammetry and chronoamperometry. With the idea to continuously exploit the high activity exhibited during cyclic voltammetry, the potential window ensured that the Pt surface is reduced back to its pristine metallic state every cycle, and the positive end was limited to before the place exchange associated with PtO_x formation, whose effect is described later below. EPC allowed sorbitol oxidation to continue at high current densities of a few milliamperes per square centimeter during the positive scan by the oxidative potentials applied transiently throughout. *SI Appendix*, Figs. S8 and S9 show examples with and without sorbitol, respectively. While sorbitol oxidation occurs above 0.4 V, the largest contribution is from potentials greater than 0.75 V (*SI Appendix*, Fig. S8*C*). With a total of 4,000 cycles applied, sorbitol oxidation proceeded at much faster rates compared with the SS

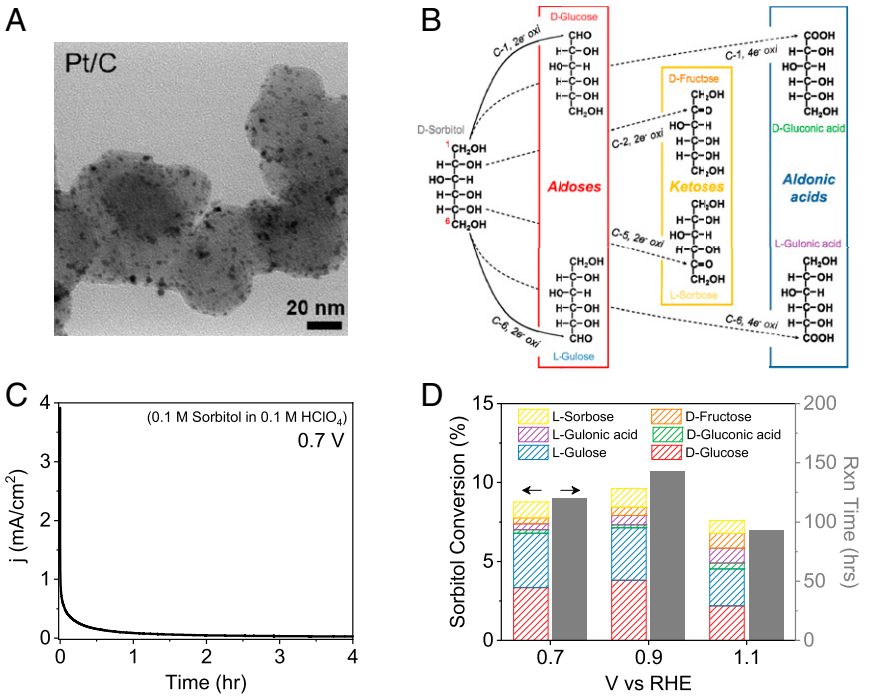

Fig. 1. Electroconversion of sorbitol by Pt/C. (*A*) Transmission electron microscopy image of Pt/C. (*B*) Electroconversion pathways to various products. The dominant pathways for Pt are the oxidation of terminal hydroxyls to aldehydes (solid lines) to form aldoses. (*C*) SS current density exhibited by Pt/C at 0.7 V (versus RHE). (*D*) Sorbitol conversion to various products (left *y*-axis) and the respective reaction times (right *y*-axis) under SS conditions at various potentials. All electrochemical measurements were conducted in a solution that was 0.1 M sorbitol and 0.1 M $HClO_4$ in water.

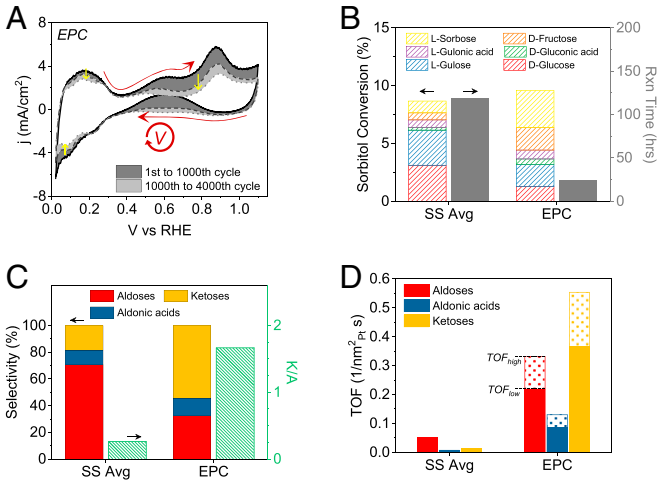

Fig. 2. EPC for sorbitol conversion. (*A*) Current density traces of EPC with a total of 4,000 cycles at 100 mV/s. Red arrows indicate the scan direction. Yellow arrows indicate the trend of current density curves throughout. (*B*) Sorbitol conversion to various products and the reaction time of EPC compared against those of the average of SS runs at 0.7, 0.9, and 1.1 V. (*C*) Product selectivity and K/A by EPC and the average of SS runs. (*D*) Comparisons of TOFs. TOF_{high} and TOF_{low} of EPC are estimated based on the average rate of the initial and final 50 cycles, respectively. Furthermore, the change of NP size from the initial (1.8 nm) to final (3.0 nm) state is considered, which reduces the available Pt surface area (estimated by hydrogen underpotential deposition) at the final state (*SI Appendix*, Fig. S12).

conversion (Fig. 2*A* and *SI Appendix*, Fig. S8*F*). Conversion of ∼10% was achieved at only a fraction of the time needed for SS runs (Fig. 2*B*). Furthermore, an unexpected improvement in ketoses selectivity was observed. K/A increased over sixfold from 0.26 (SS) to 1.67 (EPC) (Fig. 2*C* and *SI Appendix*, Fig. S10). Ketoses are produced by the oxidation of secondary hydroxyl groups as opposed to the oxidation of primary hydroxyl groups that lead to aldoses and are less likely to form because of steric hindrance and lower reactivity of the former against the latter. TOF was enhanced for all compounds by an order of magnitude between EPC and SS, and particularly for ketoses (∼40-fold) (Fig. 2*D*). Thus, we found that EPC not only significantly improved intrinsic catalytic rates but also shifted selectivity toward products known to be difficult to form using Pt by conventional SS approaches (16, 17, 32).

Throughout EPC, a gradual decline in the rate of sorbitol conversion was observed with an increasing number of cycles (Fig. 2*A*). Since EPC operates below 1.1 V, dissolution of Pt nanoparticles was not the cause as measured by inductively coupled plasma optical emission spectrometry (*SI Appendix*, Fig. S11) (34, 35). Nanoparticle coalescence and growth are observed during EPC as indicated by the loss in the Pt surface area and increase in particle size of 1.2 nm (Fig. 2*A* and *SI Appendix*, Fig. S12). However, it seems only minorly responsible for the rate decrease. As shown in *SI Appendix*, Fig. S13, replacing the used Pt/C electrode after 1,400 cycles with a new Pt/C electrode did not fully recover the initial rate observed. Such observations suggest that the gradual decrease in rate may be due to the loss of sorbitol as a reagent and the accumulation of products. Indeed, we find a similar drop when sorbitol is partially replaced with products (*SI Appendix*, Fig. S14). Therefore, the rate decline during EPC seems intrinsic to the reaction and not a result of the method itself. In addition, taking into account the change in the Pt surface area, the TOF based on the last 50 cycles (TOF_{low}) was 70% of the initial TOF based on the first 50 cycles (TOF_{high}, Fig. 2*D*).

The key feature of EPC is its high activity in contrast to that of SS conversion (Fig. 2*D*). The initial activity measured at the onset of SS conversion, despite matching closely with EPC, does not persist and is lost as a steep decay (*SI Appendix*, Fig. S5). The SS conversion was conducted to avoid nonfaradaic capacitive current contributions. Such short-lived activity may be related to charge transfer processes limited to preadsorbed species. However, the average charge passed per cycle from sorbitol oxidation during EPC (14.3 mC/cycle) requires preadsorbed sorbitol molecules in a number equivalent to that of adsorbed H at ∼106% coverage of Pt nanoparticles. This is physically not possible, considering the size difference between H and sorbitol. In addition, the majority of the Pt surface is still available for hydrogen underpotential deposition during EPC (Fig. 2*A*). Lastly, application of staircase voltammetry confirmed that the high activity during EPC did not originate from surface-limited reactions due to preadsorbed species (see *SI Appendix*, *Supplementary text* and Figs. S15–S17).

Depletion of sorbitol near the electrode as the cause of the fast activity decay during SS conversion could be ruled out as well. First, the time-dependent current density at various potentials exhibited a trend that does not match with diffusion-controlled currents (*SI Appendix*, Fig. S18). Moreover, convection induced to the electrolyte solution did not mitigate the loss of the high activity (*SI Appendix*, Fig. S19). In addition, the change in the local pH (i.e., acidification by proton release) is expected to be minor, considering the highly acidic condition used in the work as well as the geometric current densities that are far below a few tenths of milliamperes per square centimeter necessary to induce a significant pH shift (24).

The Effect of Pt Surface Oxidation. We suggest that oxidation/dehydrogenation of water by Pt leading to its surface oxidation is the main cause of the activity loss under SS conditions. Under positive potentials, the oxidative power of Pt can be applied to oxidizing water molecules, leading to surface oxidation (O_{ads} or PtO_x) (*SI Appendix*, Fig. S20) (36–38). Tracing Pt NP surface oxidation in a sorbitol-free environment shows how it progresses at various fixed potentials (Fig. 3*A*). A common feature is that the oxidative power of Pt is rapidly lost: the rate of surface oxidation quickly levels off (Fig. 3*A*). It is expected that as Pt surface oxidation progresses toward equilibrium states determined for each potential, its capacity to oxidize water (or hydroxyls) will diminish. Its fast progression is what causes the rapid loss of high oxidative activity for sorbitol as well. Accordingly, when the Pt NPs have lost their oxidative power through surface oxidation in a sorbitol-free 0.1 M $HClO_4$ under constant potential, injecting a small aliquot of concentrated sorbitol only resulted in minor activities for sorbitol oxidation (Fig. 3*B* and *SI Appendix*, Fig. S21).

To further corroborate these observations, Raman spectroscopy was used to confirm the surface oxidation occurring under SS conversion of sorbitol. Shell-isolated nanoparticle-enhanced Raman spectroscopy (SHINERS) was applied by depositing silica-coated gold nanoparticles onto polycrystalline Pt used for spectroelectrochemistry (*SI Appendix*, Fig. S22) (39, 40). Fig. 3*C* shows the Raman spectra measured at open circuit potential and various times during SS conversion at 1.2 V. At open circuit, the $*CO_{ads}$ bands from the dissociative adsorption of sorbitol were observed at 374 (bridge) and 478 (atop) cm^{-1}, which disappeared at positive potentials (*SI Appendix*, Fig. S3). When biased at 1.2 V, new bands appeared around 240, 580, and 1,160 cm^{-1} that coincided with the decay of the sorbitol conversion current (Fig. 3 *C*, *Inset*). The same bands appeared when biased at 1.2 V without sorbitol present in the solution and can be assigned to the surface oxides PtO_x formed above 1.1 V (*SI Appendix*, Fig. S23) (40). As shown in Fig. 3*D*, surface oxidation charge analysis of Pt/C in 0.1 M $HClO_4$ also indicates the formation PtO_x at potentials greater than 1.1 V (*SI Appendix*, Fig. S24). Above 1.1 V, place exchange is known to occur, thus converting Pt-O_{ads} to a surface oxide PtO_x (36–38). At SS conversions below 1.1 V, loss of oxidative activity is expected as the Pt surface oxidizes to form an equilibrium coverage O_{ads}

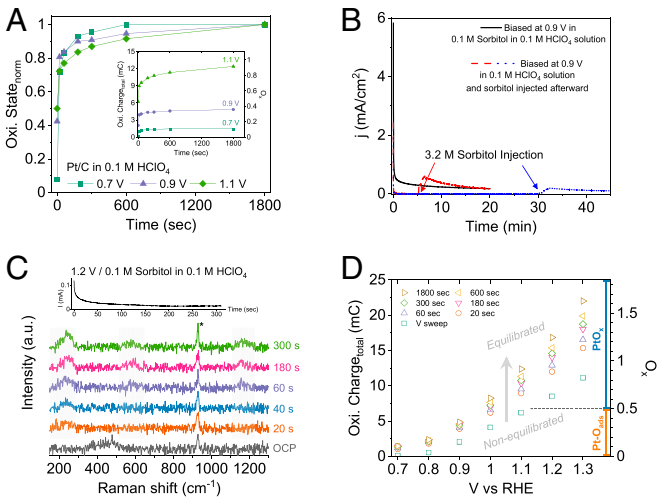

Fig. 3. Surface oxidation of Pt and its relation to sorbitol conversion. (*A*) The relative degree of oxidation normalized by the final state reached at 1,800 s for Pt/C in 0.1 M $HClO_4$ at various potentials. Inset shows the total charge passed and the associated oxygen atoms per available surface Pt atom equivalent (O_x) for Pt/C surface oxidation. The initial points are the states reached by the potential sweep (at 100 mV/s) to each potential. (*B*) Sorbitol oxidation by a prebiased Pt/C in a sorbitol-free 0.1 M $HClO_4$. Pt/C is initially biased at 0.9 V in a pure 0.1 M $HClO_4$ solution (20 mL) and 3.2 M sorbitol solution (625 μL in 0.1 M $HClO_4$) is injected near the Pt/C electrode under vigorous stirring to result in a ~0.1-M sorbitol solution (red dashed and blue dotted). The black solid curve is the original current density exhibited by Pt/C at 0.9 V in 0.1 M sorbitol in 0.1 M $HClO_4$. (*C*) SHINERS of polycrystalline Pt in 0.1 M sorbitol in 0.1 M $HClO_4$ solution at open circuit potential and during SS conversion at 1.2 V. Inset shows the current measured at 1.2 V during spectra collection. Asterisk represents the perchlorate band (929 cm^{-1}) from the electrolyte. Each spectrum was collected for 10 s. (*D*) The extent of Pt/C surface oxidation measured by the total oxidation charge and the associated oxygen atoms per available surface Pt atom equivalent (O_x) across various potentials for different periods in 0.1 M $HClO_4$. The studied periods range from the states reached by the potential sweep (at 100 mV/s) up to holding the bias for 1,800 s. Before the place exchange and formation of surface oxide PtO_x, O_{ads} can reach close to 0.5 in coverage as discussed in previous works (36, 37).

(Fig. 3*D*, *SI Appendix*, Fig. S25). Therefore, the loss of oxidative power following Pt surface oxidation toward equilibrium states causes the fast decay of sorbitol oxidation activity at each potential. Leveraging this knowledge, EPC focuses on the high oxidative power of the nonequilibrated Pt/water interface through the continuous cycling of potential involving a positive potential sweep for electrooxidation and a quick reversal to reduce the surface back to pristine Pt before reaching equilibrium.

It should be noted that restoration of the metallic Pt surface is evident from the overlapping hydrogen underpotential deposition region during consecutive cycles (*SI Appendix*, Fig. S8*B*). The gradual decline of hydrogen underpotential deposition current observed in the long term is due to particle coalescence and loss of total surface area as mentioned in the section probing changes to the Pt nanoparticles during EPC (Fig. 2*A*, *SI Appendix*, Fig. S12). Moreover, it is speculated that Pt may be less oxidized than the nonequilibrated states reached during the potential sweep in a sorbitol-free condition as can be deduced from the behavior of Pd, a Pt-group element (*SI Appendix*, Fig. S26).

Previous work suggests that the first step of sorbitol oxidation is a proton–electron transfer from the hydroxyl group to form an oxygen-bound intermediate state (41). The following proton–electron transfer from the alpha carbon ultimately generates a carbonyl. Tafel analysis of EPC suggests that the second step is rate-limiting (*SI Appendix*, Fig. S27) (42). Thus, the nonequilibrated Pt surfaces can readily oxidize the hydroxyl group in the first step, which may be expected from their capacity to strongly bind oxygen atoms. However, such capacity is lost at fixed potentials with Pt surfaces close to oxidation equilibrium, leading to a significant loss of catalytic activity.

Ketoses Formation by Electrochemical Potential Cycling. Besides the order of magnitude improvement in TOF, EPC also exhibits an increase in the ketoses production (Fig. 2). This observation is unexpected considering the selectivity observed from SS conversions as well as how Pt has been regarded as an electrocatalyst that is limited to oxidation of only terminal hydroxyl groups (17, 31). Here, we demonstrate that a nonequilibrated Pt surface with a high oxidative capacity is, however, active for secondary alcohol oxidation. Fig. 4 shows EPC applied to various polyols such as glycerol (C_3), erythritol (C_4), and ribitol (C_5). TOFs are improved by one (for aldoses) to two (for ketoses) orders of magnitude across all polyols (*SI Appendix*, Figs. S28–S30). In particular, the enhanced ketoses formation raises the K/A three- to fivefold when comparing against that of SS conversion. This result clearly suggests that there is an underutilized capacity of Pt for electrooxidation of organic compounds. The often-considered low catalytic activity of Pt is due to equilibration of its surface through surface oxidation under prolonged SS conditions rather than intrinsic inactivity. Scan-rate–dependent results of EPC also show that slower scan rates result in a decline of TOFs as well as ketoses selectivity (*SI Appendix*, Fig. S31).

Application of the nonequilibrated Pt surface for electrooxidation could be achieved analogously through short potential pulses. By the repetitive potential application between 0.02 and 1.0 V for short periods, high-rate sorbitol conversion and enhanced ketoses formation (i.e., high K/A) were observed (*SI Appendix*, Fig. S32). Moreover, it was confirmed that the small amount of $*CO_{ads}$ generated by the dissociative adsorption of sorbitol during EPC (*SI Appendix*, Fig. S3) does not play a major role in the reactivity of Pt NPs. During potential pulsing, there was a negligible formation of $*CO_{ads}$ despite similar activity for sorbitol oxidation (*SI Appendix*, Fig. S32).

Shifting the positive end of EPC above 1.1 V allows access to the nonequilibrated surface oxide PtO_x beyond the metallic Pt with low coverage of O_{ads} (Fig. 3*D*) (36–38). Its presence is connected to

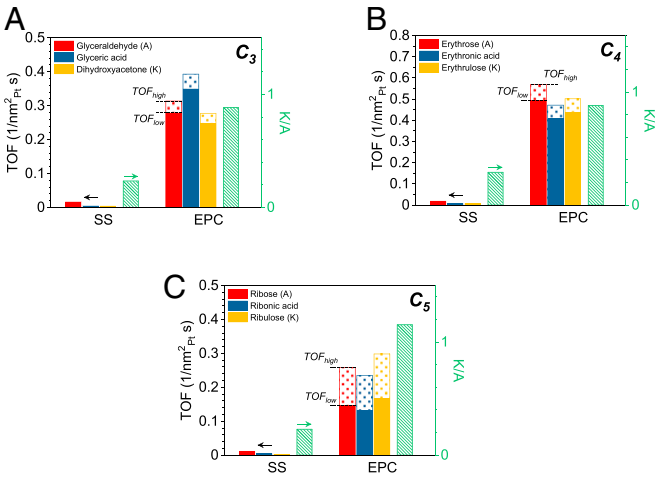

Fig. 4. Application of EPC to polyols other than sorbitol. TOFs and K/A for both SS conversion (at 0.9 V) and EPC applied to (*A*) glycerol (C_3 polyol), (*B*) erythritol (C_4 polyol), and (*C*) ribitol (C_5 polyol). TOF_{high} and TOF_{low} of EPC are estimated based on the average rate of the initial and final 50 cycles, respectively. Furthermore, the change in the available Pt surface area (estimated by hydrogen underpotential deposition) as a result of NP growth (*SI Appendix*, Fig. S12) at the final state is considered.

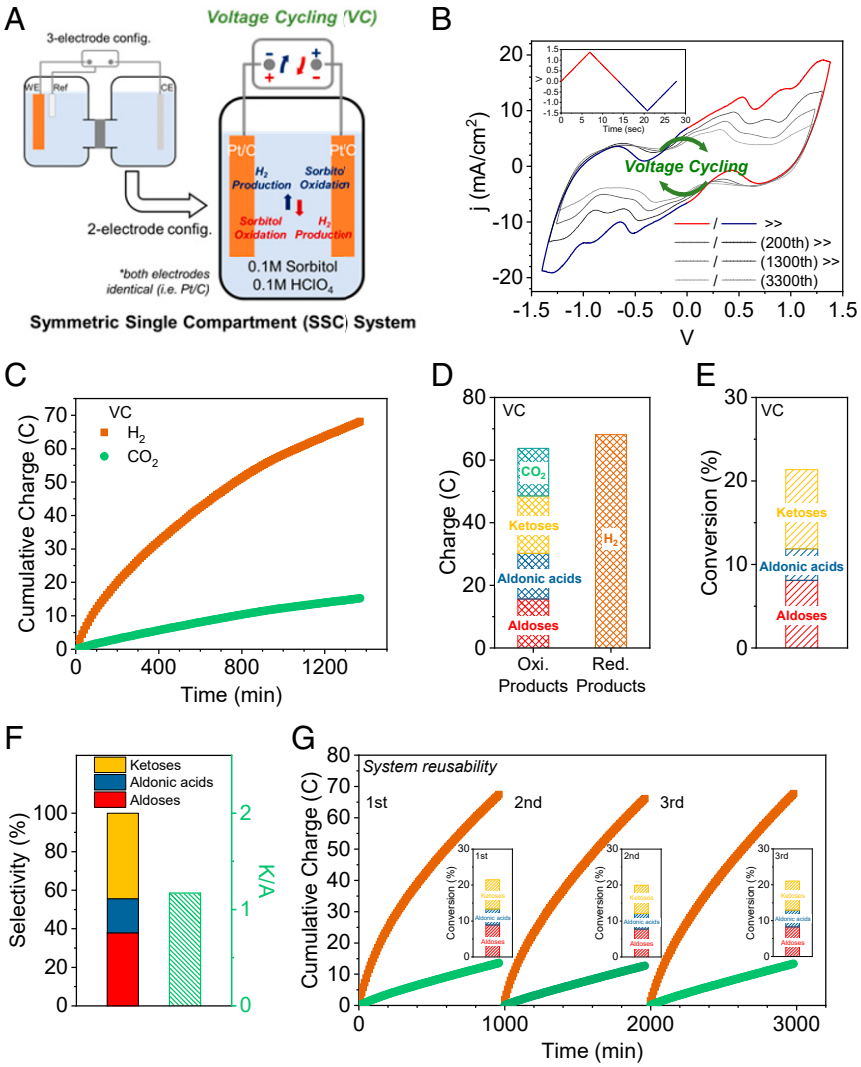

Fig. 5. VC for sorbitol conversion. (*A*) A schematic of the SSC device used and its operation under VC. It contains two identical Pt/C electrodes of 1 cm^2 geometric area at a loading of 120 $\mu g_{Pt}/cm^2$, and the electrolyte is 0.1 M sorbitol in 0.1 M $HClO_4$. (*B*) VC applied at 200 mV/s for a total of 3,300 cycles. The inset shows a single voltage scan that is applied repetitively. (*C*) Time-dependent cumulative charge equivalents for H_2 (two-electron reduction) and CO_2 (two-electron oxidation) produced by VC. (*D*) The total charge equivalents for oxidation and reduction products. Sorbitol conversion to various products (*E*) and selectivity and K/A (*F*) by VC. (*G*) Repeated uses of the same SSC device for sorbitol conversion by VC.

another high-current-density regime as shown in *SI Appendix*, Fig. S33. Furthermore, the PtO_x is reduced far below the potential range in which it is formed and thus becomes a metastable oxide during the reverse potential scan (*SI Appendix*, Fig. S20). The greater presence of such metastable PtO_x also induces a strong oxidative activity for sorbitol (*SI Appendix*, Fig. S33).

In general, all O_{ads} or PtO_x are temporarily stable during the reverse scan, and in the course of their reduction, an oxidative activity involving the hydroxyl group is observed. We find that the C_3-C_4 polyols are more oxidized in this regime compared with the C_5-C_6 polyols, which is likely due to the higher reactivity of the metastable oxidized Pt toward smaller polyols (*SI Appendix*, Figs. S28–S30). This may be the reason why, when oxidizing small alcohols such as methanol, the activity during the reverse scan is even at par with that of the forward scan (43).

As expected with nonequilibrated surfaces, EPC applied to sorbitol oxidation with the positive end at 1.3 V exhibited high TOFs (*SI Appendix*, Fig. S34). Meanwhile, aldoses selectivity increased with a K/A of 0.6. In comparison against the original EPC applied to 1.1 V, selectivity shift could be correlated with the presence of the nonequilibrated PtO_x during the forward scan (>1.1 V) and the reverse as a metastable oxide (*SI Appendix*, Fig. S34). Limiting the negative potential limit and maintaining the presence of surface oxide further amplified the selectivity shift (*SI Appendix*, Fig. S35). Therefore, selectivity seems to be dictated by the nonequilibrium surface phase present during potential cycling. As with ketoses formation, we find that the metallic Pt surface is crucial, better allowing sorbitol to adsorb and interact with the surface in a lateral configuration with more accessibility to the inner hydroxyl groups. However, under oxidizing potentials, such a state is very short-lived because of the interference of the O_{ads} that readily form, limiting the oxidation to the terminal hydroxyl groups. Further study is needed regarding the surface phase present under nonequilibrium conditions as well as its effect on the electrooxidation reactions of organic compounds.

Voltage Cycling in a Two-Electrode Electrolyzer. To make use of a catalyst or method in an applicable setting, it needs to be transferable to an electrolyzer in a two-electrode configuration. Application of continuous alteration of potentials to electrolyzers is

nontrivial, since they typically operate under a static voltage difference between the two electrodes (*SI Appendix*, Fig. S36). Therefore, despite the benefits of potential pulse applications, previous works have only focused on what occurs on the working electrode in a three-electrode configuration (18–23, 25). Doing so with the EPC approach required a certain strategy to be devised.

The need for a constant potential shift on one electrode places a constraint on the other: the second electrode has to simultaneously shift its potential, since the voltages applied are referenced to each other (*SI Appendix*, *Supplementary Text*, Fig. S37). Thus, careful consideration of the other electrode in terms of its reactions under potential alteration, the potential range required, and how both electrodes operate in a synchronized fashion is necessary for an electrolyzer to operate based on the principles of EPC. We propose a symmetric single compartment (SSC) system, in which both electrodes are identical and perform the same set of reactions in one compartment. Its example operation in a pure electrolyte solution demonstrated that both electrodes behave in a controlled manner under potential alterations (*SI Appendix*, *Supplementary Text*, Fig. S38). Then, VC, the two-electrode equivalent to the three-electrode EPC, can be successfully applied to the device (*SI Appendix*, Fig. S39). The same procedures were followed to test an electrolyte solution containing sorbitol, which proved the applicability of VC to sorbitol electrooxidation together with the coupled half-reaction of water reduction to H_2 gas (*SI Appendix*, *Supplementary Text*, Figs. S40 and S41).

The schematic of the device to utilize VC for sorbitol conversion is shown in Fig. 5*A*. Two identical Pt/C electrodes alternate between sorbitol oxidation and H_2 production, a valuable coproduct. The necessary conditions for VC to mimic EPC were confirmed as a continuous voltage scan in between ±1.4 V (*SI Appendix*, Fig. S42). Fig. 5*B* shows the current density curves as a result. The positive scan (red) oxidized sorbitol on one electrode, while H_2 was produced at the other electrode. The same occurred on the negative scan (blue) with the potential signs and the roles of the two electrodes switched. The absolute scan width |V| in both directions was dynamically reduced during VC to accommodate changes in the ohmic loss from the steadily declining current density (*SI Appendix*, Fig. S43).

Production of H_2 was confirmed and measured throughout (Fig. 5*C*). The overall charge balance in the system was approximately closed considering that the amount of reductive charge used for H_2 production was very close to the sum of oxidative charges required to form carbon-containing products in the liquid phase or as CO_2 (Fig. 5*D*). Over 20% of sorbitol conversion to products was demonstrated by VC (Fig. 5*E*). It also exhibited a rate order of magnitude higher compared with a typical operation under static voltage application (*SI Appendix*, Fig. S44). In addition, undesirable humin formation occurred under the static voltage condition, representing an additional issue for its application toward sorbitol electroconversion. In contrast, VC did not show signs of humin production (*SI Appendix*, Figs. S44 and S45). VC was also able to promote ketoses formation as demonstrated with EPC (Fig. 5*F*).

We tested the reusability of the system by replacing the sorbitol-containing electrolyte postreaction with a fresh solution and applying VC for multiple rounds. The tests resulted in production rates mostly unaltered for at least three consecutive cycles (Fig. 5*G* and *SI Appendix*, Fig. S46). It is because not only VC operates at potentials at which Pt NP dissolution is negligible (*SI Appendix*, Fig. S11) but also because NP coalescence and growth mostly occur at the smallest initial size and slow down as particles grow (*SI Appendix*, Fig. S47). Furthermore, nanoparticle size in the range of 2 to 5 nm does not seem to critically affect the catalytic behavior under these conditions.

Conclusion

Through the adoption of an electrochemical approach called voltage cycling, while using standard Pt nanoparticles as catalysts, we have demonstrated high-rate polyol electrolysis coupled with H_2 production. The fundamentals of the method are anticipated to be applicable to various feedstocks and biomass-derived compounds for electrochemical conversion. Moreover, by taking advantage of the latest advances in nanoscience, such as imposing certain structural characteristics (e.g., morphology and composition) to nanoparticles closely linked to their catalytic behavior (e.g., adsorption strength and durability), the approach demonstrated here has much room for further development.

Materials and Methods

Pt/C Working Electrode Preparation for a Three-Electrode Configuration. Pt/C (Premetek, 20% Pt on Vulcan) is dispersed in ethanol (0.4 mg_{Pt}/mL) by sonication. The homogeneous Pt/C solution is drop-casted onto a 1 cm^2 carbon paper support (Sigracet) at a loading of 40 $\mu g_{Pt}/cm^2$ and dried under ambient conditions over 24 h.

Electrochemical Experiments in a Three-Electrode Configuration. All measurements are conducted in an H cell with the two compartments separated by a Nafion membrane (*SI Appendix*, Fig. S2). Pt/C loaded on carbon paper (40 $\mu g_{Pt}/cm^2$, 1 cm^2_{geo}) is used as a working electrode (Pt area estimated by hydrogen underpotential deposition is 32.2 cm^2_{Pt}). A reversible hydrogen electrode (RHE) is used as a reference electrode, while a platinum wire is used as a counter electrode. The working compartment contains 0.1 M sorbitol (Sigma-Aldrich, 99%) in a 0.1-M $HClO_4$ solution, and the counter compartment only contains 0.1 M $HClO_4$. For direct comparisons, tests are also conducted with the working compartment containing only 0.1 M $HClO_4$ (without sorbitol). The working compartment is sparged with Ar gas before the start of any electrochemical measurement for >15 min, and the Ar purge (20 standard cubic centimeters per minute) continues throughout the measurement. The working compartment is stirred using a magnetic stir bar.

Voltammetry sweeps (linear sweep voltammetry and cyclic voltammetry) are conducted at a scan rate of 100 mV/s unless stated otherwise. Chronoamperometry tests are conducted following a few cyclic voltammetry scans in the range of 0.02 to 1.3 V until stabilization and ending the scan at the selected potential of interest to continue into SS current measurement right afterward (e.g., cyclic voltammetry ending at 0.7 V before continuing chronoamperometry at 0.7 V). This eliminates current contributions from the rapidly decaying nonfaradaic capacitive current that is proportional to ΔV [= V_2(applied) − V_1(prior)] at early periods of chronoamperometry. For all measurements in this three-electrode configuration, 85% of the ohmic loss (typical solution resistance: ~10 Ohm) is compensated by the potentiostat (Biologic) in real time.

For experiments that involve product analysis, faradaic efficiency (%) is estimated by the amount of charge needed to produce each product i ($Q_{product,i}$) divided by the total charge (Q_{total}) passed.

$$\text{FE}(\%)\ \text{of product}\ i = 100 \times \frac{Q_{\text{product},i}}{Q_{\text{total}}} = 100 \times \frac{n_{e,\text{product}\,i} \times C \times N_{\text{product},i}}{Q_{\text{total}}}$$

($n_{e,product\,i}$: # of electrons involved for oxidation to product i (e.g., $n_{e,glucose} = 2$)-
C : Faraday constant 96,485 $\frac{C}{mol}$, $N_{product,i}$: mols of product i).

Conversion (%) to each product is estimated as follows:

$$\text{Conversion to product}\ i\,(\%) = 100 \times M_{\text{product},i} / M_{\text{sorbitol}}$$

($M_{product,i}$: conc. of product i, $M_{sorbitol} = 0.1$ M).

Selectivity (%) to each product group is estimated as follows:

$$\text{Selectivity}(\%) = 100 \times M_{\text{product}} / M_{\text{total}}$$

($M_{product}$: $M_{aldoses}$ or $M_{aldonic\ acids}$ or $M_{ketoses}$, $M_{total} = \sum M_{product}$).

TOF is estimated as follows:

$$\text{TOF}_{\text{product}} = \frac{N_A \times N_{\text{product}}}{\text{Area}_{Pt} \times \text{total reaction time}}$$

(N_A : Avogadro constant, $N_{product}$: mols of product,

Area_{Pt} : *Pt* area estimated by H UPD, $3.22 \times 10^{15} \text{nm}^2_{Pt}$).

Note that Area_{Pt} remains the same for steady-state runs confirmed by H-UPD.

EPC. A standard EPC run is conducted in the identical three-electrode H-cell configuration (*SI Appendix*, Fig. S2). It is performed by scanning the potential of the Pt/C working electrode in between 0.02 and 1.1 V at 100 mV/s. A single cycle is a complete potential scan that consists of both the positive sweep from 0.02 to 1.1 V and the negative sweep back to 0.02 V. A total of 4,000 cycles is performed with the products in liquid phase analyzed by HPLC-MS and the gas product (i.e., CO_2) measured at the outlet in regular intervals by gas chromatography. TOF_{high} and TOF_{low} are calculated by estimating $N_{product}$ of the first and last 50 cycles, respectively, based on the amount of charge passed for each compared against the total charge passed and considering the total amount of products detected. While TOF_{high} is based on the initial area of Pt NPs, TOF_{low} takes into account the growth of particles during EPC (*SI Appendix*, Fig. S12) and their final area being 0.66 of the initial area estimated by H-UPD. This relative change in the area matches closely with the estimate based on average particle size increase (approximately 40% loss of initial area). As TOF represents intrinsic activity, the amount of time spent in between 0.02 and 0.35 V in the H-UPD region during EPC is not considered as part of the reaction time for TOF estimation purposes only (otherwise, the reaction time plotted in figures, such as Fig. 2*B*, is the actual total time spent for the entire EPC run).

Product Analysis. Sorbitol oxidation products dissolved in the liquid phase (electrolyte solution) are analyzed by HPLC-MS instrumentation (Waters). The HPLC system runs using a binary gradient pump and an autosampler with a 20-μL sample loop. Since the products are not suited for ultraviolet–visible absorption (i.e., their major functionality being hydroxides) or refractive index detection (i.e., too-low concentration below the detection limit of refractive index detector), an MS (electrospray ionization with single quadrupole mass detection) is used for their analysis. Product separation is carried out in an LC column (XBridge Bridged Ethylene Hybrid Amide XP 2.5 μm, 3 mm × 150 mm) and the mobile phase is LC-MS grade 90% acetonitrile/10% water with 0.08% NH_4OH (volume by volume percentage) at a flow rate of 1 mL/min. The MS operates in electrospray mode with capillary voltage 2.8 kV, cone voltage 25 V, source temperature 120 °C, desolvation temperature 350 °C, desolvation gas flow 550 L/h, and cone gas flow 50 L/h. Sample injection volume is 20 μL, and each sample is prepared by diluting the original solution (i.e., standard analytes and electrolysis reaction solutions) by a factor of 1/125 in an LC-MS grade 75% acetonitrile/25% water (volume by volume percentage). The calibration standards of known concentrations are prepared in the same electrolyte (i.e., 0.1 M $HClO_4$) solution and are regularly tested each day before sample testing to ensure that sensitivity factors are accurate.

For electrolysis runs that require detection and quantification of CO_2 and H_2 gas, the gas outlet is connected to a gas chromatograph (Buck Scientific) equipped with a thermal conductivity detector (TCD) and flame ionization detector (FID) to sample gaseous products. They are separated by HayeSep D and Molsieve 5A columns under Ar as a carrier gas and at a temperature of 45 °C. H_2 gas is measured by the TCD, and CO_2 passes through a methanizer tube before being detected by the FID.

Surface Oxidation Analysis of Pt/C. Pt/C loaded on carbon paper is used as a working electrode in an H cell filled with 0.1 M $HClO_4$. RHE is used as a reference electrode, and the working compartment is constantly purged with Ar gas at 20 sccm. Surface oxidation charge during the potential sweep (at 100 mV/s) to each potential is estimated by integrating the charge under the surface oxidation curve in the voltammogram (≥0.7 V) with the double-layer charging current as the baseline (*SI Appendix*, Fig. S20*A*). The surface oxidation charge at different times for each potential is estimated by following the identical procedure as the chronoamperometry tests for sorbitol conversion: the potential sweep to the selected potential is immediately followed by a fixed potential application for different time periods (e.g., CV ending at 0.7 V and then continuing CA at 0.7 V). At the end of each period, a reverse potential sweep to the H-UPD region is conducted to reduce the Pt surface with prolonged times for surface oxidation, resulting in a larger total charge for reduction (*SI Appendix*, Fig. S20*B*). The additional reduction charge measured by comparing against the reverse potential sweep without the fixed potential application is added to the surface oxidation charge during the potential sweep (V sweep) to estimate the total oxidation charge as a function of time and potential. The oxygen atoms per available surface Pt atom equivalent (O_x) are estimated by dividing the total oxidation charge to the twice the amount of the H-UPD charge (6.755 mC), assuming one-to-one correlation of the underpotential deposited H and the surface Pt atoms.

In Situ Electrochemical Raman Spectroscopy. The silica-coated gold nanoparticles ($Au@SiO_2$) were prepared following the Frens method to prepare the gold nanoparticles and coat a thin layer of silica (39, 40, 44). In short, a gold nanoparticle (55 nm size) solution was prepared by injecting 1 weight percent (wt. %) sodium citrate solution into a boiling 0.01 wt.% $HAuCl_4$ solution. Then, 30 mL gold nanoparticle solution was first injected with 0.4 mL 3-aminopropyltrimethoxysilane (1 mM) and stirred for 15 min at room temperature. A total of 3.2 mL sodium silicate solution (0.54 wt.%, pH 10.2 to 10.3) was added and stirred for 3 min. The solution was transferred to a water bath (90 °C) and stirred for 20 min. Afterward, the solution was cooled down in an ice bath and centrifuged at 5,500 rpm for 15 min for washing and redispersion.

$Au@SiO_2$ were deposited on a polycrystalline Pt wire electrode and dried under vacuum. The $Au@SiO_2$-deposited Pt electrode was cleaned by applying −2.0 V versus Ag/AgCl in a neutral electrolyte solution multiple times (45). Then, it was transferred to a spectroelectrochemical cell filled with Ar-purged 0.1 M $HClO_4$ or 0.1 M sorbitol in 0.1 M $HClO_4$. Raman spectra were recorded with Xplora Plus confocal Raman microscope (HORIBA) using an He–Ne laser with a wavelength of 637.8 nm. The spectrometer was calibrated using a Si wafer. Each spectrum was collected for 10 s.

VC in an SSC System. The SSC device consists of two identical Pt/C (120 $\mu g_{Pt}/cm^2$, 1 cm^2_{geo}) electrodes facing each other in a single compartment that contains a 10-mL solution of 0.1 M sorbitol in 0.1 M $HClO_4$. Both electrodes are prepared from a solution of Pt/C (Premetek, 20% Pt on Vulcan) dispersed in ethanol (0.4 mg_{Pt}/mL) by sonication. The compartment is constantly purged with Ar (10 sccm), and the gas outlet is connected to a GC. For preliminary testing of the device in a three-electrode configuration (*SI Appendix*, Fig. S42), an RHE is used as a reference and placed at the center between the two Pt/C electrodes. Otherwise, in a two-electrode configuration, the voltage (V) applied is the applied bias between the two electrodes. The resistance between the reference and either Pt/C electrode is ∼10 ohm (the total resistance between the two Pt/C electrodes is ∼20 ohm). Voltage is scanned at 200 mV/s in between +1.4 V and −1.4 V, and throughout a total of 3,300 cycles, the positive and negative ends of V applied are reduced (final voltage ±1.22 V) to accommodate changes in the V_{IR} (*SI Appendix*, Fig. S43).

Data Availability. All study data are included in the article and/or *SI Appendix*.

ACKNOWLEDGMENTS. This work was mostly supported by seed funding from the Global Climate and Energy Program at Stanford University. Part of the work was supported by a research grant (9455) from The Villum Foundation. M.C. acknowledges additional support from a Sloan Fellowship. M.Z. acknowledges support from the US Department of Energy (DOE), Office of Science, Basic Energy Sciences, under Contract No. DE-AC02-05CH11231. The Lawrence Berkeley National Laboratory Catalysis Facility is supported by DOE under the same contract number. Part of this work was performed at the Stanford Nano Shared Facilities, supported by the NSF under Award ECCS-2026822. The authors thank Angel Yang and Sunmoon Yu for helpful discussions on product and elemental analysis.

1. F. B. Bendixen *et al.*, Industrial hydrogen production. *Science* **759**, 756–759 (2019).
2. P. De Luna *et al.*, What would it take for renewably powered electrosynthesis to displace petrochemical processes? *Science* **364**, eaav3506 (2019).
3. S. Chu, Y. Cui, N. Liu, The path towards sustainable energy. *Nat. Mater.* **16**, 16–22 (2016).
4. R. F. Service, Renewable bonds. *Science* **365**, 1236–1239 (2019).
5. Z. J. Schiffer, K. Manthiram, Electrification and decarbonization of the chemical industry. *Joule* **1**, 10–14 (2017).
6. H. G. Cha, K. S. Choi, Combined biomass valorization and hydrogen production in a photoelectrochemical cell. *Nat. Chem.* **7**, 328–333 (2015).
7. B. You, X. Liu, N. Jiang, Y. Sun, A general strategy for decoupled hydrogen production from water splitting by integrating oxidative biomass valorization. *J. Am. Chem. Soc.* **138**, 13639–13646 (2016).
8. T. Li, Y. Cao, J. He, C. P. Berlinguette, Electrolytic CO_2 reduction in tandem with oxidative organic chemistry. *ACS Cent. Sci.* **3**, 778–783 (2017).
9. R. S. Sherbo, R. S. Delima, V. A. Chiykowski, B. P. MacLeod, C. P. Berlinguette, Complete electron economy by pairing electrolysis with hydrogenation. *Nat. Catal.* **1**, 501–507 (2018).
10. R. S. Kim, Y. Surendranath, Electrochemical reoxidation enables continuous methane-to-methanol catalysis with aqueous Pt salts. *ACS Cent. Sci.* **5**, 1179–1186 (2019).

11. D. Liu *et al*., Selective photoelectrochemical oxidation of glycerol to high value-added dihydroxyacetone. *Nat. Commun.* **10**, 1779 (2019).
12. W. R. Leow *et al*., Chloride-mediated selective electrosynthesis of ethylene and propylene oxides at high current density. *Science* **368**, 1228–1233 (2020).
13. Z. W. She *et al*., Combining theory and experiment in electrocatalysis: Insights into materials design. *Science* **355**, eaad4998 (2017).
14. M. B. Ross *et al*., Designing materials for electrochemical carbon dioxide recycling. *Nat. Catal.* **2**, 648–658 (2019).
15. Y. Kwon, Y. Birdja, I. Spanos, P. Rodriguez, M. T. M. M. Koper, Highly selective electrooxidation of glycerol to dihydroxyacetone on platinum in the presence of bismuth. *ACS Catal.* **2**, 759–764 (2012).
16. H. Kimura, K. Tsuto, T. Wakisaka, Y. Kazumi, Y. Inaya, Selective oxidation of glycerol on a platinum-bismuth catalyst. *Appl. Catal. A Gen.* **96**, 217–228 (1993).
17. Y. Kwon, E. de Jong, J. K. van der Waal, M. T. M. Koper, Selective electrocatalytic oxidation of sorbitol to fructose and sorbose. *ChemSusChem* **8**, 970–973 (2015).
18. C. W. Lee, N. H. Cho, K. T. Nam, Y. J. Hwang, B. K. Min, Cyclic two-step electrolysis for stable electrochemical conversion of carbon dioxide to formate. *Nat. Commun.* **10**, 3919 (2019).
19. A. Engelbrecht *et al*., On the electrochemical CO_2 reduction at copper sheet electrodes with enhanced long-term stability by pulsed electrolysis. *J. Electrochem. Soc.* **165**, J3059–J3068 (2018).
20. R. M. Arán-Ais, F. Scholten, S. Kunze, R. Rizo, B. Roldan Cuenya, The role of in situ generated morphological motifs and Cu(i) species in C2+ product selectivity during CO_2 pulsed electroreduction. *Nat. Energy* **5**, 317–325 (2020).
21. J. Gopeesingh *et al*., Resonance-promoted formic acid oxidation via dynamic electrocatalytic modulation. *ACS Catal.* **10**, 9932–9942 (2020).
22. D. E. Blanco, B. Lee, M. A. Modestino, Optimizing organic electrosynthesis through controlled voltage dosing and artificial intelligence. *Proc. Natl. Acad. Sci. U.S.A.* **116**, 17683–17689 (2019).
23. C. Wattanakit, T. Yutthalekha, S. Asssavapanumat, V. Lapeyre, A. Kuhn, Pulsed electroconversion for highly selective enantiomer synthesis. *Nat. Commun.* **8**, 2087 (2017).
24. J. C. Bui, C. Kim, A. Z. Weber, A. T. Bell, Dynamic boundary layer simulation of pulsed CO_2 electrolysis on a copper catalyst. *ACS Energy Lett.* **6**, 1181–1188 (2021).
25. H. Sakaguchi, H. Matsumura, H. Gong, Electrochemical epitaxial polymerization of single-molecular wires. *Nat. Mater.* **3**, 551–557 (2004).
26. H. Kobayashi *et al*., Synthesis of sugar alcohols by hydrolytic hydrogenation of cellulose over supported metal catalysts. *Green Chem.* **13**, 326–333 (2011).
27. J. J. Bozell, G. R. Petersen, Technology development for the production of biobased products from biorefinery carbohydrates—the US Department of Energy's "Top 10" revisited. *Green Chem.* **12**, 539 (2010).
28. M. Besson, P. Gallezot, C. Pinel, Conversion of biomass into chemicals over metal catalysts. *Chem. Rev.* **114**, 1827–1870 (2014).
29. Z. Zhang, G. W. Huber, Catalytic oxidation of carbohydrates into organic acids and furan chemicals. *Chem. Soc. Rev.* **47**, 1351–1390 (2018).
30. L. F. A. Proença *et al*., On the oxidation of d-sorbitol on platinum single crystal electrodes: A voltammetric and in situ FTIRS study. *Electrochim. Acta* **44**, 735–743 (1998).
31. L. Proença *et al*., Electrocatalytic oxidation of d-sorbitol on platinum in acid medium: Analysis of the reaction products. *J. Electroanal. Chem. (Lausanne)* **432**, 237–242 (1997).
32. C. Coutanceau, S. Baranton, R. S. B. Kouamé, Selective electrooxidation of glycerol into value-added chemicals: A short overview. *Front Chem.* **7**, 100 (2019).
33. Y. Kwon, K. J. P. Schouten, M. T. M. Koper, Mechanism of the catalytic oxidation of glycerol on polycrystalline gold and platinum electrodes. *ChemCatChem* **3**, 1176–1185 (2011).
34. A. A. Topalov *et al*., Dissolution of platinum: Limits for the deployment of electrochemical energy conversion? *Angew. Chem. Int. Ed. Engl.* **51**, 12613–12615 (2012).
35. S. Cherevko, A. R. Zeradjanin, G. P. Keeley, K. J. J. Mayrhofer, A comparative study on gold and platinum dissolution in acidic and alkaline media. *J. Electrochem. Soc.* **161**, H822–H830 (2014).
36. G. Jerkiewicz, G. Vatankhah, J. Lessard, M. P. Soriaga, Y. S. Park, Surface-oxide growth at platinum electrodes in aqueous H_2SO_4: Reexamination of its mechanism through combined cyclic-voltammetry, electrochemical quartz-crystal nanobalance, and Auger electron spectroscopy measurements. *Electrochim. Acta* **49**, 1451–1459 (2004).
37. K. Sasaki, N. Marinkovic, H. S. Isaacs, R. R. Adzic, Synchrotron-based in situ characterization of carbon-supported platinum and platinum monolayer electrocatalysts. *ACS Catal.* **6**, 69–76 (2016).
38. J. Drnec *et al*., Initial stages of Pt(111) electrooxidation: Dynamic and structural studies by surface X-ray diffraction. *Electrochim. Acta* **224**, 220–227 (2017).
39. J. F. Li *et al*., Surface analysis using shell-isolated nanoparticle-enhanced Raman spectroscopy. *Nat. Protoc.* **8**, 52–65 (2013).
40. Y. F. Huang, P. J. Kooyman, M. T. M. M. Koper, Intermediate stages of electrochemical oxidation of single-crystalline platinum revealed by in situ Raman spectroscopy. *Nat. Commun.* **7**, 12440 (2016).
41. L. Proença, M. I. S. I. S. Lopes, I. Fonseca, F. Hahn, C. Lamy, An in situ IR reflectance spectroscopic study of the electro-oxidation of d-sorbitol on platinum. *Electrochim. Acta* **44**, 1423–1430 (1998).
42. Y. H. Fang, Z. P. Liu, Tafel kinetics of electrocatalytic reactions: From experiment to first-principles. *ACS Catal.* **4**, 4364–4376 (2014).
43. C. Tan *et al*., A self-supporting bimetallic Au@Pt core-shell nanoparticle electrocatalyst for the synergistic enhancement of methanol oxidation. *Sci. Rep.* **7**, 6347 (2017).
44. G. Frens, Controlled nucleation for the regulation of the particle size in monodisperse gold suspensions. *Nat. Phys. Sci (Lond.)* **241**, 20–22 (1973).
45. J.-F. Li, A. Rudnev, Y. Fu, N. Bodappa, T. Wandlowski, In situ SHINERS at electrochemical single-crystal electrode/electrolyte interfaces: Tuning preparation strategies and selected applications. *ACS Nano* **7**, 8940–8952 (2013).